

Magnetic phase diagram of a spin-1 condensate in two dimensions with dipole interactionJonas A. Kjäll,¹ Andrew M. Essin,¹ and Joel E. Moore^{1,2}¹*Department of Physics, University of California, Berkeley, California 94720, USA*²*Materials Sciences Division, Lawrence Berkeley National Laboratory, Berkeley, California 94720, USA*

(Received 15 September 2009; revised manuscript received 9 November 2009; published 8 December 2009)

Several new features arise in the ground-state phase diagram of a spin-1 condensate trapped in an optical trap when the magnetic-dipole interaction between the atoms is taken into account along with confinement and spin precession. The boundaries between the regions of ferromagnetic and polar phases move as the dipole strength is varied and the ferromagnetic phases can be modulated. The magnetization of the ferromagnetic phase perpendicular to the field becomes modulated as a helix winding around the magnetic field direction with a wavelength inversely proportional to the dipole strength. This modulation should be observable for current experimental parameters in ⁸⁷Rb. Hence the much-sought supersolid state with broken continuous translation invariance in one direction and broken global $U(1)$ invariance, occurs generically as a metastable state in this system as a result of dipole interaction. The ferromagnetic state parallel to the applied magnetic field becomes striped in a finite system at strong dipolar coupling.

DOI: [10.1103/PhysRevB.80.224502](https://doi.org/10.1103/PhysRevB.80.224502)

PACS number(s): 03.75.Kk, 03.75.Mn, 03.75.Lm

I. INTRODUCTION

Bose condensates of atoms with nonzero total spin $F \geq 1$ show various phases combining magnetic and superfluid order. When the magnetic symmetry is broken spontaneously, as can occur when the atoms are confined in a spin-independent optical trap, condensates are classified as “polar” (for antiferromagnetic interactions) or “ferromagnetic.” Most theoretical studies of these spinor Bose condensates neglect the long-range interaction between atomic magnetic moments and this neglect is justified for many experimental conditions. However, recent experiments^{1–3} investigating ordering in a nearly two-dimensional (2D) condensate have shown complex magnetic behavior in the ferromagnetically interacting $F=1$ spinor Bose gas of ⁸⁷Rb.

The most surprising feature of these experiments, which image the spin distribution in real space, is a long-lived phase that appears to have the broken global $U(1)$ invariance of a superfluid along with possible breaking of the continuous translational symmetry in one or two directions, i.e., with stripelike or checkerboardlike order. A possible supersolid phase has recently also been suggested in the superfluid of ⁴He.⁴ Many theoretical papers have been written about the properties of ⁴He and whether a supersolid phase can exist in the absence of disorder. Only recently have theoretical studies been done to explain the observed supersolidlike behavior in a ⁸⁷Rb spinor condensate.⁵ The earlier studies of ⁸⁷Rb concentrated on magnetic properties arising from the weak spin-dependent local interaction and the quadratic Zeeman shift. More recent experiments^{2,3} indicates that the long-range dipole interaction also plays an important role in the formation of the magnetic phases in spatially large systems and with this addition a supersolid state might be possible.

Most previous studies of this system concern dynamical properties: the leading instability when the Hamiltonian is changed to favor ferromagnetic order can be stripelike or checkerboardlike depending on parameters.^{5–7} In this paper, our goal is to determine the static ground-state phase diagram. We start from the phases that are well established at low temperatures^{8–11} for a spin-1 gas with no dipole interaction and quadratic Zeeman effect. (Low temperatures mean

below the superfluid and magnetic transitions where all the studies in this paper will take place.) We then add the dipole interaction to see how it changes the phases as well as the location of the boundary between them. We do this in a quasi-two-dimensional geometry as in the experiments.^{1–3} We investigate both an infinite and a finite square planar geometry. After observing the formation of two kinds of stripe order in a Monte Carlo simulation, we developed an analytical approach to explain the results, based upon smallness of the dipolar coupling at short distances. That analytical approach is presented first in order to prepare the groundwork for the simulation results.

We show that all boundaries in the phase diagram, except between the two polar phases, are moved when the dipole interaction is added, some in a nonintuitive way. The magnetic-dipole interaction prefers a ferromagnetic state but the confinement makes a ferromagnetic state out of the plane energetically unfavorable. Moreover, the spin precession make the in-plane perpendicular ferromagnetic state unfavorable since the spin rotates out of the plane. Both ferromagnetic phases can get modulated in one direction. The phase parallel to the external fields needs a strong dipole interaction or a system much wider than its length to become modulated. This modulation appears as fully magnetized stripes with sharp domain walls between them. The phase perpendicular to the external fields gets modulated, from the very lowest dipole strengths, into a helical configuration around the field. The wavelength of the helix is inversely proportional to the dipole strength. For ⁸⁷Rb the wavelength is $\sim 80 \mu\text{m}$ and should be observable in experiments.

The outline of this paper is as follows. In the following section, we review the basic physics of spinor condensates without the dipole interaction. In Sec. III we introduce the dipole interaction and put it into a form that is convenient for numerical simulations. Section IV presents analytical results in the limit of weak dipole interaction and Sec. V contains the results of our Monte Carlo simulations of the problem. The final section summarizes the relationship between our results and those of other theoretical papers and suggests how future experiments could be designed to observe clearly the metastable supersolid phase found in our simulations.

II. REVIEW OF SPINOR CONDENSATE WITHOUT MAGNETIC DIPOLE INTERACTION

A Bose-Einstein condensate (BEC) of spin $F=1$ atoms is described by a three-component complex order parameter

$$\Psi(\mathbf{x}) = \sqrt{n_{3D}(\mathbf{x})} \psi(\mathbf{x}) = \sqrt{n_{3D}(\mathbf{x})} \begin{pmatrix} \psi_{+1}(\mathbf{x}) \\ \psi_0(\mathbf{x}) \\ \psi_{-1}(\mathbf{x}) \end{pmatrix}, \quad (1)$$

where the spinor $\psi(\mathbf{x})$ is normalized as $\psi^\dagger \psi = 1$ and the subscripts label the spin eigenvalue with respect to an arbitrarily chosen quantization direction. In the absence of external fields and neglecting the dipole interaction, the Hamiltonian governing the condensate is^{8,9}

$$H_0 = \int d^3x \left[\frac{\hbar^2}{2m} |\nabla \Psi|^2 + \frac{c_0}{2} n_{3D}^2 + \frac{c_2}{2} n_{3D}^2 M^2 \right], \quad (2)$$

where m is the atomic mass, $\mathbf{M}(\mathbf{x}) = \psi^\dagger(\mathbf{x}) \mathbf{F} \psi(\mathbf{x})$ is the dimensionless magnetization ($|\mathbf{M}| \leq 1$), and $\{F^i\}$ are the three generators of $SU(2)$ in the spin-1 representation

$$F^x = \frac{1}{\sqrt{2}} \begin{pmatrix} 0 & 1 & 0 \\ 1 & 0 & 1 \\ 0 & 1 & 0 \end{pmatrix}, \quad F^y = \frac{1}{\sqrt{2}} \begin{pmatrix} 0 & -i & 0 \\ i & 0 & -i \\ 0 & i & 0 \end{pmatrix},$$

$$F^z = \begin{pmatrix} 1 & 0 & 0 \\ 0 & 0 & 0 \\ 0 & 0 & -1 \end{pmatrix}. \quad (3)$$

The first term in the Hamiltonian is the kinetic energy for bosons with mass m . The next two terms are the spin-independent and spin-dependent contact interactions, respectively. The coefficients are given by $c_0 = (4\pi\hbar^2/3m)(2a_2 + a_0)$ and $c_2 = (4\pi\hbar^2/3m)(a_2 - a_0)$ with $\{a_0, a_2\}$ the s -wave scattering lengths in the channel with total angular momentum $\{0, 2\}$.

When $c_2 < 0$ (ferromagnetic) it is energetically favorable for this system to magnetize, $M \neq 0$, while $c_2 > 0$ favors a ‘‘polar’’ state with $M=0$. The scattering lengths for ⁸⁷Rb are $a_0 = 101.8a_B$ and $a_2 = 100.4a_B$,¹² where a_B is the Bohr radius so c_2 is negative and its condensate will be ferromagnetic in the absence of external fields (still neglecting the dipole interaction). However, the condensate of ²³Na will be in a polar state.⁸

The external fields normally applied to a spinor condensate consist of an optical trap and a uniform magnetic field described by the following addition to the Hamiltonian

$$H_{ef} = \int d^3x [U + q\psi^\dagger(\hat{\mathbf{B}} \cdot \mathbf{F})^2 \psi] n_{3D}. \quad (4)$$

The trapping potential $U(\mathbf{x})$ confines the condensate spatially; for our purposes, its main effect will be to produce a quasi-two-dimensional geometry. The quadratic Zeeman shift q can be tuned independently of \mathbf{B} with microwave radiation, $q = q^B + q^{EM}$.¹³ We take the two sources as coaxial along $\hat{\mathbf{z}}$ so we can use Eq. (4). This is also the axis we quantize the spinor along. The magnetic field also creates a linear Zeeman term $\mathbf{B} \cdot \int d^3x n_{3D} \boldsymbol{\mu}$ that favors an uniformly

magnetized condensate. However, experiments on ⁸⁷Rb have not observed any tendency toward such relaxation over the accessible time scales of several seconds,¹³ making the longitudinal component of magnetization conserved. (This assumption does not apply in condensates of higher spin, such as chromium.¹⁴) Normally, this component is chosen to vanish initially and can hence be ignored for the purpose of energetics. However, the magnetic field also causes Larmor precession of the magnetization perpendicular to it. This is an important effect that needs to be taken into account as it modifies the nature of the magnetic interaction on time scales longer than the precession time.

The spin state of the condensate is governed by the parameters c_2 and q as in Fig. 2.¹⁵ There are two different kinds of polar states ($c_2 > 0$), one that minimizes $\langle (F^z)^2 \rangle = 0$ and one that maximizes $\langle (F^z)^2 \rangle = 1$ the impact of the quadratic Zeeman term. Respectively,

$$\psi_{\parallel}^P(\phi) = e^{i\phi} \begin{pmatrix} 0 \\ 1 \\ 0 \end{pmatrix}, \quad \psi_{\perp}^P(\phi, \theta) = \frac{e^{i\phi}}{\sqrt{2}} \begin{pmatrix} -e^{-i\theta} \\ 0 \\ e^{i\theta} \end{pmatrix}. \quad (5)$$

Consequently, does the phase P_{\parallel} , with order-parameter manifold $U(1)$, appears at $q > 0$, while the phase P_{\perp} appears when $q < 0$. Note that the range of θ is only $[0, \pi)$, or alternatively that the order-parameter manifold for this phase is $U(1) \times U(1)/Z_2$.¹⁶ When $c_2 < 0$ and $q < 0$, both energies are minimized by ferromagnetic states

$$\psi_{\parallel, \uparrow}^F(\phi) = e^{i\phi} \begin{pmatrix} 1 \\ 0 \\ 0 \end{pmatrix}, \quad \psi_{\parallel, \downarrow}^F(\phi) = e^{i\phi} \begin{pmatrix} 0 \\ 0 \\ 1 \end{pmatrix} \quad (6)$$

giving a manifold $U(1) \times Z_2$ (recall that we exclude the linear Zeeman energy from energetic considerations), see Fig. 1. In the final quadrant of the phase diagram, however, no ferromagnetic state minimizes the quadratic Zeeman energy. The smallest impact of a ferromagnetic state on the quadratic Zeeman term is $\langle (F^z)^2 \rangle = 1/2$ for

$$\psi_{\perp}^F(\phi, \xi) = \frac{e^{i\phi}}{2} \begin{pmatrix} e^{-i\xi} \\ \sqrt{2} \\ e^{i\xi} \end{pmatrix}. \quad (7)$$

Consequently, for $q < q_c = 2|c_2|n_{3D}$ the state will be a linear combination of ψ_{\parallel}^P and ψ_{\perp}^F with magnetization $M_x + iM_y = \sqrt{1 - (q/q_c)^2} e^{i\xi}$ and manifold $U(1) \times U(1)$, see Fig. 1. Above q_c , the state will be the pure polar state P_{\parallel} .

Typical experimental values for ⁸⁷Rb (Ref. 1–3) include a peak density of $n_0 = 2.5 \times 10^{14} \text{ cm}^{-3}$, giving the interaction strengths $c_0 n_0 = 1.9 \text{ kHz}$ and $c_2 n_0 = -9 \text{ Hz}$, while $q^B \approx 1.6 \text{ Hz}$ and q^{EM} can be tuned from roughly -50 to 50 Hz and is normally taken coaxial to q^B .¹³

A. Confinement

The optical trap in the experiment makes the gas effectively two dimensional with a Thomas-Fermi radius $r_{TF} \approx 1.5 \mu\text{m}$ along the direction of tightest confinement.^{1–3} Since this is smaller than the spin-healing length ξ

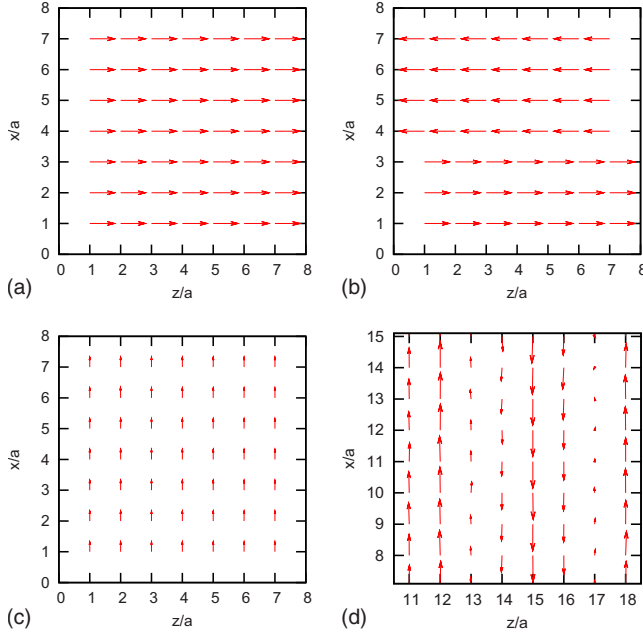


FIG. 1. (Color online) Examples of possible spin configurations in the plane. The external fields are along the horizontal axis, $M_z(x, z)$ is plotted on the horizontal axis, $M_x(x, z)$ is on the vertical for every plaquette, and $M_x(x, z)$ is not shown. (a) Uniform fully magnetized F_{\parallel} , (b) striped fully magnetized F_{\parallel} , (c) uniform partly magnetized F_{\perp}/P_{\parallel} state, and (d) helical fully magnetized F_{\perp} .

$= \sqrt{\hbar^2/(2m|c_2|n_{3D})} \approx 2.5 \mu\text{m}$, we take the confinement to be along the \hat{y} direction and treat the gas as frozen along this direction; that is, we take

$$\Psi(\mathbf{x}) = \sqrt{n_{2D}(x, z)}\rho(y)\psi(x, z), \quad (8)$$

where we assume $\int dy \rho(y) = 1$. In the following we will consider one of two profiles $\rho(y)$ as convenient, a boxcar profile and a Gaussian

$$\rho_1(y) = \frac{1}{K} \Theta(K/2 - y) \Theta(K/2 + y), \quad \rho_2(y) = \frac{1}{\sigma_y} \sqrt{\frac{2}{\pi}} e^{-2y^2/\sigma_y^2}, \quad (9)$$

where $\Theta(x)$ is the Heaviside step function. We introduce a common notation for the condensate thickness T and a three-dimensional (3D) density $\bar{n}_{3D}(x, z)$ without y dependence

$$\frac{1}{T} = \langle \rho \rangle = \int dy \rho(y)^2, \quad \bar{n}_{3D}(x, z) = \frac{n_{2D}(x, z)}{T} \quad (10)$$

for the boxcar profile and for the Gaussian profile, to be able to treat both profiles simultaneously in Sec. IV. In most of our analysis these densities are also independent of (x, z) , except where we use a nonzero trapping potential $U(x, z)$ in the plane.

B. Precession

Atoms with magnetic moment $\boldsymbol{\mu}_{\perp} = g_F \mu_B \mathbf{M}_{\perp}$ perpendicular to the field precess at frequency $|\gamma|B_0 = |g_F| \mu_B B_0$ around the fields. As usual, μ_B is the Bohr magneton and g_F is

Lande's g factor. For ^{87}Rb , $g_F = -1/2$ and a field of $B_0 = 150 \text{ mG}$ produces a Larmor precession at 110 kHz, a scale orders of magnitude larger than the contact interactions or the quadratic Zeeman energy.

The Hamiltonian considered so far is invariant under the spin rotation

$$\psi_k(x, z) \rightarrow U_{kl}(t) \psi_l(x, z), \quad U(t) = e^{-i\gamma B_0 \hat{\mathbf{B}} \cdot \mathbf{F} t} \quad (11)$$

and is hence unaffected by the rapid Larmor precession. Therefore, adding precession does not affect the phase diagram in the problem with only local interactions.^{8,9} However when we include the dipole interaction in the next section, both confinement and spin precession become important.

III. MAGNETIC-DIPOLE INTERACTION

The interactions considered thus far for a spin-1 condensate are all local. However, the moments $\boldsymbol{\mu}$ will interact through the long-ranged dipole interaction. This is weak for ^{87}Rb relative to most other energies in the system but since it is long ranged it will have an important impact on the magnetic phases. The initial studies of the spin-1 condensate ignored this term^{8,15} but some recent works have included it along with the effects of quasi-two-dimensional confinement and rapid Larmor precession.^{5,6} Among other results, it was shown that dipolar interaction renders the Larmor precession unstable⁶ and we return to this point in the concluding section. Until then we follow previous authors and assume that this instability has significant effects only at late times and so neglect it. Cherng and Demler examined the instability spectrum of a uniform ferromagnetic state within a mean-field and collective-mode analyses. We will use the same physical model but instead look at the ground-state phase diagram and consider a wider range of parameters c_2 , q , and c_d [see Eq. (12) below] with analytical and Monte Carlo calculations.

The total Hamiltonian we work with is

$$H = H_0 + H_{ef} + H_{dip}, \quad (12)$$

where

$$H_{dip} = \frac{c_d}{2} \int d^3x d^3x' n_{3D}(\mathbf{x}) M_i(\mathbf{x}) n_{3D}(\mathbf{x}') M_j(\mathbf{x}') \times \left[\nabla_i \nabla'_j \frac{1}{|\mathbf{x} - \mathbf{x}'|} - \frac{4\pi}{3} \delta_{ij} \delta^{(3)}(\mathbf{x} - \mathbf{x}') \right]. \quad (13)$$

This is the same as the more usual expression with $(\delta_{ij} - 3\hat{r}_i\hat{r}_j)/r^3$ but split it into a part that is positive-(semi)definite and a part that simply shifts the parameter $c_2 \rightarrow c_2 - 4\pi c_d/3$ (see the beginning of Appendix A for a fuller discussion of the magnetic-dipole term). Indeed, with two integrations by parts the first term becomes the Coulomb interaction for a charge density $\nabla \cdot (n_{3D} \mathbf{M})$. We will typically mean just this term when referring to “the dipole interaction” since it is the difficult part. The strength of the dipole term is given by $c_d = \mu_0 g_F^2 \mu_B^2 / 4\pi$, where μ_0 is the vacuum permeability, giving a value of $c_d n_0 = 0.8 \text{ Hz}$ for ^{87}Rb . The effect of confinement is less trivial for this term than for the others and transforming to a rotating frame is also nontrivial since

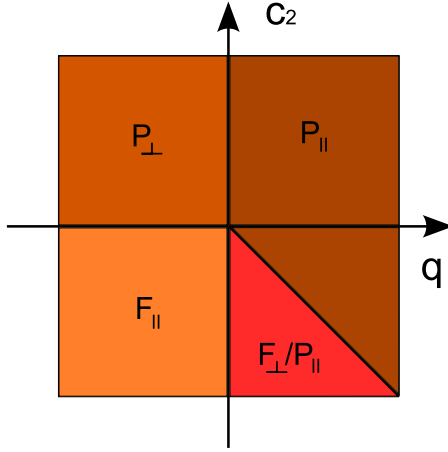


FIG. 2. (Color online) Ground-state phase diagram of a spin-1 condensate without dipolar interaction; from Mukerjee *et al.* (Ref. 15).

the interaction couples spin directions to spatial directions. See Appendix A for a full treatment of these effects. In the following section, we discuss how the dipole interaction is expected to modify the phase diagram when it is sufficiently weak that the $H_{dip}=0$ ground states can be used as a starting point.

IV. ANALYTICAL RESULTS

Adding the dipole interaction Eq. (13) will change the phase diagram [Fig. 2]. The term that looks like the spin-dependent interaction will just move the whole phase diagram up along c_2 with $\frac{4\pi c_d}{3}$. The energy from the Coulomb part of the dipole interaction is always positive hence this part prefers a polar state with zero magnetization $M=0$. Consequently, regions of Fig. 2 with polar states above $c_2 = \frac{4\pi c_d}{3}$ will not change if we add the dipole-dipole coupling. However, the rest of the phase diagram may be affected and the phase boundaries will depend on c_d as we now discuss in some detail.

A. Weak dipole interaction

Adding a weak dipole term (weak compared to the kinetic-energy term) will only change the phase diagram slightly. We start out by ignoring any new phases and investigate how a weak dipole interaction will move the boundaries between the existing phases. The three magnetic terms in the Hamiltonian are the spin-dependent contact interaction, the quadratic Zeeman, and the dipole term. By comparing the energy contributions from these three for simple *Ansätze* we can locate the boundaries between different minima, in a system with L the extent along z and W the extent along x .

The polar phases are, of course, the simplest [see Eq. (5)]

$$E^{P_{\parallel}} = 0, \quad E^{P_{\perp}} = q\bar{n}_{3D}LWT. \quad (14)$$

Consider next the phase F_{\parallel} , which appeared at $q, c_2 < 0$ in the system without dipolar energy. The effective charge density

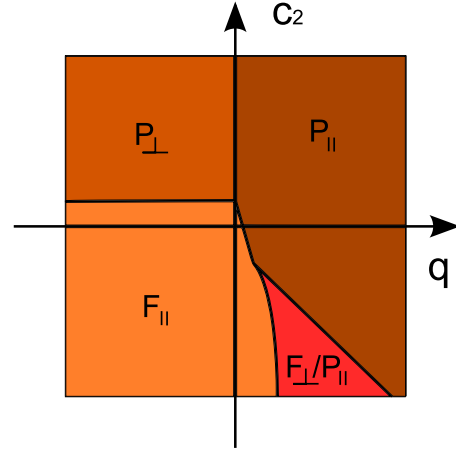


FIG. 3. (Color online) Ground-state phase diagram for a spin-1 condensate with dipole interaction and external fields that introduces a quadratic Zeeman term and rapid spin precession. Both polar and ferromagnetic phases appear perpendicular as well as parallel to the field.

for such a state describes two quasi-one-dimensional lines of charge located at $\pm L/2$, of length W . The self-energy of such lines of charge is given by $2c_d(\bar{n}_{3D}M)^2WT^2 \ln W/T$, see Appendix C, to leading order. The other two terms are easily kept exact. Keeping terms of order A^2 and $A \ln A$ where $A = L, W$, [see Eq. (6)]

$$E^{F_{\parallel}} = \frac{\tilde{c}_2}{2}\bar{n}_{3D}^2LWT + q\bar{n}_{3D}LWT + 2c_d\bar{n}_{3D}^2WT^2 \ln W/T \quad (15)$$

with $\tilde{c}_2 = c_2 - 4\pi c_d/3$.

The transition in the left half plane between the states F_{\parallel} and P_{\perp} , see Fig. 3, will hence be moved up from $c_2=0$ for a system without dipole interaction to

$$c_{2c} \equiv 4c_d \left(\frac{\pi}{3} - \epsilon_L \right), \quad (16)$$

where $\epsilon_L = \frac{\ln W/T}{L/T}$ will vanish in the large-system limit.

The region of the phase diagram with $q > 0$ and $c_2 < 0$ is the most interesting due to the rapid precession of the perpendicular magnetization about the magnetic field and the high dipolar-energy cost of spins pointing out of the plane. Consequently, the region of F_{\perp}/P_{\parallel} in the phase diagram will shrink and the regions of P_{\parallel} and F_{\parallel} grow with the latter extending to positive values of q . For a uniform condensate with spins out of the plane, the Coulomb energy is equivalent to that of a parallel-plate capacitor, giving an energy $2\pi c_d(\bar{n}_3M)^2T^2LW/T$ to leading order, i.e., neglecting fringing fields, see Appendix C.

Because of the precession, the spins will effectively average the out-of-plane and in-plane interaction energies with equal weights. Consequently, the dipole energy for magnetization perpendicular to the external fields is $c_d(\bar{n}_3M)^2(\pi W + T \ln L/T)LT$. To find the energy for the F_{\perp}/P_{\parallel} state, we first have to find M since this state is not completely magnetized. Consider a spinor $\psi^T = (a, b, a)$ with $a = \sqrt{(1-b^2)/2}$

($1/\sqrt{2} < b < 1$), which represents a superposition of ψ_{\parallel}^P and ψ_{\perp}^F [see Eqs. (5) and (7)]. Its magnetization is $M_x = 2b\sqrt{1-b^2}$. Putting it all together

$$E^{F_{\perp}/P_{\parallel}} = 4b^2(1-b^2) \left[\frac{\tilde{c}_2}{2}W + c_d(\pi W + T \ln W/T) \right] \bar{n}_{3D}LT + q\bar{n}_{3D}(1-b^2)LWT. \quad (17)$$

The energy for this state is minimized at

$$b^2 = \frac{1}{2} \left(1 + \frac{q}{q_c} \right). \quad (18)$$

As the notation suggests, the transition between the phases P_{\parallel} and F_{\perp}/P_{\parallel} occurs at $q=q_c$, where $E^{F_{\perp}/P_{\parallel}}=E^{P_{\parallel}}=0$ and $M=0$

$$q_c \equiv 2|c_2|\bar{n}_{3D} - 4c_d\bar{n}_{3D} \left(\frac{\pi}{3} + \epsilon_w \right), \quad (19)$$

where $\epsilon_w = \frac{\ln L/T}{W/T}$ will vanish in the large-system limit. As can be seen in Eqs. (18)–(20), the value of the magnetization and hence the order parameter for the F_{\perp}/P_{\parallel} state decreases continuously and is zero at the phase transition to the P_{\parallel} state

$$M_0 = |\langle F_{\perp}/P_{\parallel} \rangle| = \sqrt{1 - (q/q_c)^2}. \quad (20)$$

This is exactly the same equation as for a system without dipole interaction, except that q_c now is given by Eq. (19). Plugging the form for b , Eqs. (18) and (19), back in also allow us to locate the transition between F_{\perp}/P_{\parallel} and F_{\parallel} , where $E^{F_{\perp}/P_{\parallel}}=E^{F_{\parallel}}$, which will occur at

$$q_{c2} \equiv \sqrt{q_c \left[2|c_2|\bar{n}_{3D} + 8c_d\bar{n}_{3D} \left(\frac{\pi}{3} - 2\epsilon_L \right) \right]} - q_c. \quad (21)$$

Finally, the transition between F_{\parallel} and P_{\parallel} will take place when $E^{F_{\parallel}}=E^{P_{\parallel}}=0$, at

$$q_{c3} \equiv \frac{|c_2|\bar{n}_{3D}}{2} + 2c_d\bar{n}_{3D} \left(\frac{\pi}{3} - \epsilon_L \right). \quad (22)$$

The three transition lines (q_c , q_{c2} , and q_{c3}) separating the three phases in the lower right quadrant meet at the point

$$(q, c_2) = 4c_d \left[\bar{n}_{3D} \left(\frac{\pi}{3} + \epsilon_w - 2\epsilon_L \right), \left(\frac{\pi}{3} + 2\epsilon_w - \epsilon_L \right) \right]. \quad (23)$$

To finish the phase diagram, we see that the transition line in Eq. (22), that separates F_{\parallel} and P_{\parallel} , can be extended to the region $q, c_2 > 0$, with the substitution $|c_2| \rightarrow -c_2$ and that it will intersect with the transition line in Eq. (16) at the point $(q, c_2) = (0, c_{2c})$.

B. Magnetization textures

The dipolar energy favors spatially modulated ferromagnetic states, which screen the long-ranged interaction, over uniform states. Consider the state F_{\parallel} . We can adapt a classic

argument of Kittel concerning the formation of magnetic domains to the present quasi-two-dimensional geometry.¹⁷ The boundary energy $2c_d\bar{n}_{3D}^2WT^2 \ln W/T$ from before will become $2c_d\bar{n}_{3D}^2WT^2 \ln d/T$ if the uniform state breaks up into Ising-type domains of width d and length L that alternate between $M_z=1$ and $M_z=-1$, keeping the total magnetization $M_0=1$ everywhere, see Fig. 1. There will be a cost in kinetic energy at the domain walls and the competition between these two effects sets the domain size.

We can estimate an upper bound for the domain-wall energy by assuming its width is the spin-healing length ξ_s . The energy will scale with the area of the wall $\sim LT$ and the surface density will be $\sigma_w \sim \hbar^2\bar{n}_{3D}/2m\xi_s$. With the number of domains given by W/d , the energy is

$$E = \sigma_w \frac{LWT}{d} + 2c_d\bar{n}_{3D}^2WT^2 \ln d/T, \quad (24)$$

which gives

$$d^{\parallel} = \frac{\sigma_w}{c_d\bar{n}_{3D}^2T}L. \quad (25)$$

The resulting domains have a width proportional to the length of the system and are very large when the dipolar coupling is weak. In ⁸⁷Rb with the experimental parameters given in Sec. II A, $\sigma_w \sim 10^4$ Hz μm^{-1} and $d^{\parallel} \sim 20$ L , which could be difficult to achieve experimentally.

For a rectangular sample ($L > W$) in the F_{\parallel} state with a constraint of zero total longitudinal magnetization $\{\int dx n_{3D}(\mathbf{x})M^z(\mathbf{x})=0\}$, it can be more energetically favorable to split up into two domains perpendicular to the field. The energy for this configuration is $E=2\sigma_wWT + 3c_d\bar{n}_{3D}^2WT^2 \ln W/T$ to leading order and if this is lower than the energy in Eq. (21) it will occur. However, this is only due to the constraint; a domain-free configuration has lower energy and a configuration with several domain walls perpendicular to the field will not be favorable for any values in the phase diagram.

For the F_{\perp} state, a different modulation will appear. In particular, since the state is XY-like (the rapid Larmor precession gives the same energy for all perpendicular spin directions), it can adopt a smoothly varying magnetization texture. The smoothest form will be a helix with wave vector along the magnetic field, see Fig. 1. In other words, as shown in Fig. 4, the magnetization will adopt a configuration such as $M_x(z) = \sin(k_z z)$ and $M_y(z) = \sin(k_z z + \frac{\pi}{2})$ at any instant of time. The kinetic energy of such a state goes as k_z^2 while the dipole energy turns out to decrease as k_z for small k_z ; see Appendix B for details.

At leading order in the dipole strength, then

$$k_z^{\perp} \sim \frac{1}{\lambda_z^{\perp}} \sim \frac{c_d\bar{n}_{3D}T}{\hbar^2/2m} \quad (26)$$

with λ_z^{\perp} the wavelength of the helical modulation, for a derivation see Appendix C. In ⁸⁷Rb with experimentally accessible densities the wavelength is approximately 80 μm and should be observable. Note that the scales for the two textures are related by $d^{\parallel} \sim \lambda_z^{\perp}(L/\xi_s)$.

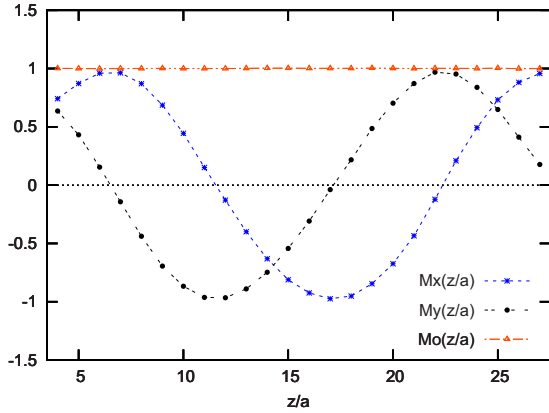


FIG. 4. (Color online) Transverse magnetization as a function of z , from numerical simulation. Orange (triangles): magnitude of total magnetization M_0 , blue (stars): transverse magnetization in plane M_x , and black (disc): transverse magnetization out of plane M_y . A helical modulation with wavelength $\lambda \approx 85 \mu\text{m}$ is clearly visible. Simulation values: $|\tilde{c}_2|\bar{n}_{3D}=320 \text{ Hz}$, $c_d\bar{n}_{3D}=0.8 \text{ Hz}$, and $q=100 \text{ Hz}$ (edges removed).

Since the modulations of F_{\parallel} and F_{\perp} decrease the total energy of those states, their regions of the phase diagram, Fig. 3, will be larger than predicted in the previous subsection. However, the dipole strength must be large to introduce domains into the F_{\parallel} state; and the energy gain in a helical texture relative to a uniform F_{\perp} is small; so the phase boundaries will not change significantly at weak or moderate dipole strengths when we take these textures into account.

V. NUMERICAL RESULTS

We investigate numerically the ground-state phase diagram of a spin-1 condensate in external fields that give rise to a quadratic Zeeman shift and Larmor precession. The Metropolis algorithm¹⁸ allows us to efficiently locate minima of a given energy functional. We discretize the system on a lattice and for the fundamental move we draw random deviations in the six real components of the field Ψ from a normal distribution at a lattice site. The initial state is similarly generated from random normally distributed variables.

A wide variety of simulation parameters (N , a , σ_y , T_{MC} , T_{MF}^c , μ , and c_0 , see below), for example, $1 \times 1 < N < 50 \times 50$, have been used to investigate the phase diagram (c_2, q, c_d) . Energies have been calculated in Hz and the lengths have been inserted in μm . Unless otherwise noted, numerical results presented here use lattice constant $a=4 \mu\text{m}$, thickness $\sigma_y=2 \mu\text{m}$, and a system size of $N=30 \times 30$ plaquettes. We also add a chemical potential to the energy, $\mu=1202 \text{ Hz } \mu\text{m}^{-2}$, in order to reproduce the experimental density for $c_0=1.9 \text{ kHz}$. Finally, we set $T_{MC}=23 \text{ nK}$ in the Metropolis weight $e^{-(H)/kT_{MC}}$, which strikes a good balance between reducing fluctuations and achieving convergence in a reasonable computation time and use a critical mean-field temperature $T_{MF}^c=100T_{MC}$.

The phase diagram we have mapped out numerically agrees well with the results presented so far. In particular, we have confirmed that the ferromagnetic states develop modu-

lations governed by the strength of the dipole interaction.

The algorithm described above tends to get trapped in local energy minima with varying densities of domain walls in the F_{\parallel} region of the phase diagram. We can, however, locate the global minimum fairly confidently by starting the system in a variety of modulated states (striped or checkerboard) and comparing the final energies. The existence of metastable states as a consequence of dipolar interactions has been discussed before for spinor condensates in an optical lattice.¹⁹ We have not observed any tendencies for the simulation in the F_{\perp}/P_{\parallel} region of the phase diagram to be trapped in a local energy minima, regardless of the initial configuration. This is as expected since any possible local ground-state configuration [Eq. (7)] can smoothly turn into another unlike in the F_{\parallel} case [Eq. (6)]. This symmetry between the two transverse components of the magnetization is present in the Hamiltonian without the dipole interaction removed by the dipole interaction and finally restored by the rapid Larmor precession. However, even if the relaxational dynamics of the Metropolis algorithm used here does not apparently get trapped in a local minimum in this phase, the actual dynamics of the experimental system is primarily precessional rather than relaxational, which could lead to metastable states.

A. Domain walls in F_{\parallel}

Near the transition $q_{c2}(c_2, c_d)$, Eq. (21), magnetization vortices with unit spin winding develop all the way along all domain walls, see Fig. 5. The vortices are alternating elliptical and hyperbolic Mermin-Ho vortices with ferromagnetic cores.^{8,20} The density of vortices increases with increasing dipole interaction, i.e., more domain walls appear and the longitudinal length of each vortex decreases. The transverse length of the vortices increases with increasing quadratic Zeeman strength up to the transition line, which can be seen in the Fourier transform of the magnetization

$$M_z(k_x) = \sum_{r,s} e^{-irk_x} M_z(r,s) \quad (27)$$

as a rise in $M_y(k_z^{\text{max}})$; see Fig. 5 on the F_{\parallel} side of the transition. The transition at q_{c2} itself remains sharp and no vortices are observed for $q > q_{c2}$. At a given instant in time does the perpendicular magnetization in all vortices in a domain boundary point in a specific direction. The correlations between the direction of the transverse magnetization of vortices in different domain walls are however weaker.

B. Boundaries and trapping potential

Finite-size effects and the details of the trapping potential seem to have little impact on our results. The only finite-size effect observed with hard-wall boundaries is a decrease in magnetization at the $z=\pm L/2$ boundaries in the transition from F_{\parallel} to P_{\perp} as shown in Fig. 6. The approximative location of this transition line from the analytical calculation, Eq. (16), is $|\tilde{c}_2|\bar{n}_{3D}=3.4 \text{ Hz}$.

We have also carried out simulations with an elliptical trap potential of the form $U(\mathbf{x})=U[v_z(\frac{z}{a})^2+v_x(\frac{x}{a})^2]$, typically

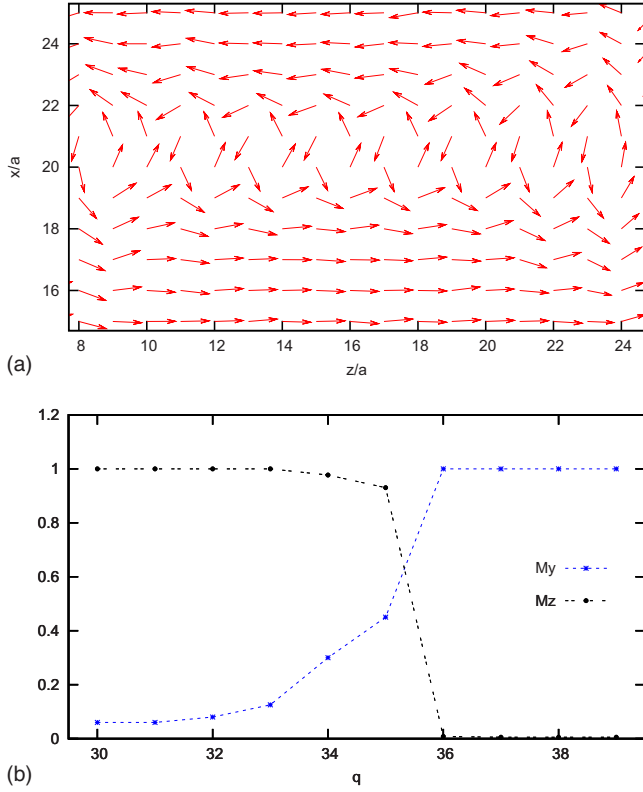


FIG. 5. (Color online) Transition to F_{\perp}/P_{\parallel} from F_{\parallel} . For q slightly smaller than (a) q_{c2} , large Mermin-Ho vortices appear between the stripes (plaquette size $a=4 \mu\text{m}$). $M_z(x, z)$ is plotted on the horizontal axis, $M_x(x, z)$ on the vertical axis, and $M_y(x, z) \approx 0$ for the whole region shown at this instant. Consequently, the maximum value of the Fourier transform of the magnetization out of plane $M_x(k_z^{\text{max}})$, see Eq. (27), increase before the (b) phase transition. Simulation variables: $|\tilde{c}_2|\bar{n}_{3D}=450$ Hz and $c_d\bar{n}_{3D}=7.2$ Hz, and (a) $q=35$ Hz and (b) $q=30-39$ Hz.

with $U=625 \text{ Hz } \mu\text{m}^{-2}$ and $v_z, v_x=1-10$ to more closely model experimental conditions.¹⁻³ These simulations have shown no effect other than a decrease in the density and thereby related effects as in the original paper of Ho on spinor condensates in optical traps.⁸ For example, the wavelength of the helical modulation in F_{\perp}/P_{\parallel} is inversely proportional to the density, see Fig. 7 which shows a change in wavelength through the condensate as the density changes. In particular, we have not seen the effect reported by Vengalattore *et al.*³ in which the modulation wave vector is not aligned with the applied magnetic field but is instead influenced by the orientation of the trap.

VI. DISCUSSION

We have mapped out the complete phase diagram for the model we have considered. Although the region occupied by the phase F_{\perp}/P_{\parallel} moves and shrinks with the introduction of the dipole interaction, we find that it remains accessible at physical values of $|c_2|$ and c_d in ^{87}Rb , for some values of the quadratic Zeeman shift q . Hence, by tuning q for ^{87}Rb appropriately, the three phases F_{\parallel} , F_{\perp}/P_{\parallel} , and P_{\parallel} should be observable in experiments. We also find that a spatial modu-

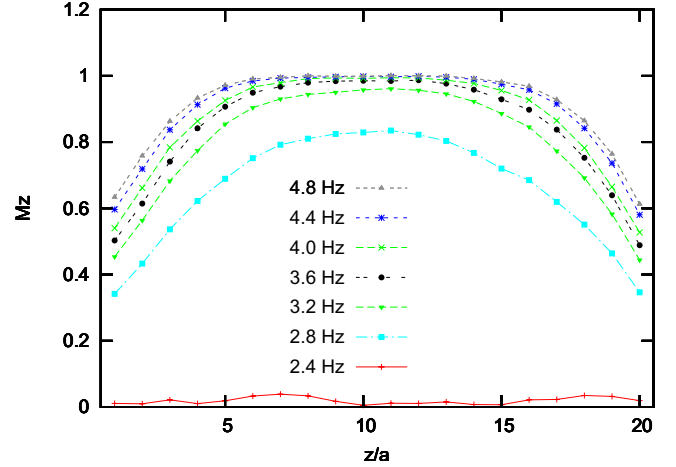


FIG. 6. (Color online) Transition to P_{\perp} from F_{\parallel} . The parallel magnetization $M_z(z/a)$ is plotted for different values of $|\tilde{c}_2|\bar{n}_{3D}=2.4-4.8$ Hz as a function of z/a . Around the transition point is the magnetization lowered at the boundaries for a finite system. Simulation values: $N=20 \times 20$, $c_d\bar{n}_{3D}=5.7$ Hz, and $q=-4$ Hz.

lations should be seen in at least the second of those phases.

There are some disagreements between our result and other results obtained theoretically and more important experimentally. The length scale in the experiment is smaller than the pitch of the helical modulation we describe above by a factor of 10, roughly, for typical parameters. Cherng and Demler⁵ find a dynamical instability at a scale nearer that seen in the experiment. That picture would suggest that even if the phase diagram obtained here describes the system at long times, the experimental system might instead reach a long-lived metastable state. As explained in Sec. V above while we do see metastable states in some parts of the phase diagram, we do not see metastable checkerboard states in the region probed by current experiments but this could be because the Metropolis dynamics of our simulation is not the actual dynamics of the condensate even if their thermodynamics are the same.

One challenge for this dynamical scenario is that in experiments, an imposed helical configuration with pitch λ

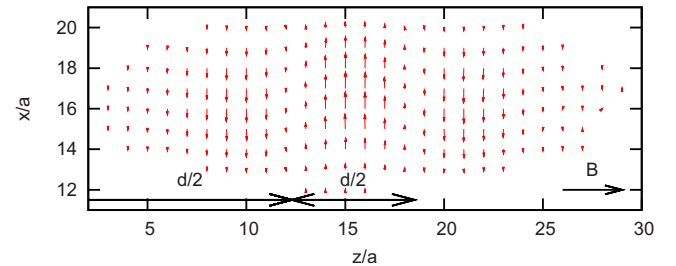


FIG. 7. (Color online) Simulation of a helical-modulated magnetized condensate in an elliptical trap. $\bar{n}_{3D}(x, z)M_z(x, z)$ is plotted on the horizontal axis, $\bar{n}_{3D}(x, z)M_x(x, z)$ on the vertical axis, and $M_y(x, z)$ is a quarter of a wavelength ahead of $M_x(x, z)$ as in Fig. 4, but is not shown. The wavelength $\lambda(z)$ of the helical modulation increases with decreasing density along the longitudinal axis. The distance between two neighboring nodes is shown; the node to the left of them is outside the graph. Simulation parameters: $v_z=1$, $v_x=10$, $|c_2|\bar{n}_{3D}=540$ Hz, $c_d\bar{n}_{3D}=1.6$ Hz, and $q=120$ Hz.

$\approx 50\text{--}150 \mu\text{m}$ (Ref. 2) quickly evolves into a state modulated at a smaller scale, again roughly ten times smaller than the stable, or at least metastable, supersolid state we predict.^{2,3} This suggests that effects we have not taken into account prevent the current experimental system from finding this minimum. As an example, it is known that the dipole interaction makes the Larmor precession unstable, according to Lamacraft,⁶ as a result, the Larmor-averaged energy that is the main focus of the present work might not be an accurate description for long times.

In order to observe the predicted supersolid clearly, our results suggest that the key is to suppress this Larmor instability while at the same time preserving the conservation of total magnetization in the field direction. The Larmor instability⁶ grows exponentially from thermal excitation of an initial perturbation at the Larmor frequency ω_L . Hence the time scale to reach a fixed final size of the instability is proportional to $\hbar\omega_L/(k_B T)$ and can be increased either by increasing the magnetic field or decreasing the temperature. At the same time, an experiment should be designed to preserve the magnetization along the field direction for as long as possible, which requires a high degree of trap uniformity. One motivation for continued exploration of this system is that our results show that the Larmor-averaged system does have a supersolid ground state for a wide range of parameters.

Note added. As this work was being prepared for submission, two e-prints appeared investigating the same experiment by slightly different approaches.^{20,21} The first, by Zhang and Ho, also investigates the static properties of ⁸⁷Rb using a deterministic numerical method and also gets the F_{\parallel} state and a modulated F_{\perp} state. The main difference between their results and ours appears to be that they find a stripe phase rather than a helix for the phase with spins perpendicular to the applied magnetic field. They find arrays of elliptical and hyperbolic Mermin-Ho vortices as a metastable dynamical state between the stripes for the F_{\parallel} state for all q . However, they are smaller than the spin-healing length and hence unobservable in our simulation although we do see them close to the transition to the F_{\perp}/P_{\parallel} state. The second, by Kawaguchi *et al.*, finds a doubly periodic (checkerboard) spin pattern as a long-lived intermediate state through a combination of mean-field theory and numerical simulation of precession-averaged equations of motion. By adding energy dissipation to the dynamics, they reach a stationary state similar to ours.

ACKNOWLEDGMENTS

The authors thank Subroto Mukerjee, Dan Stamper-Kurn, Mukund Vengalattore, Kater Murch, Jennie Guzman, Andre Wenz, Ari Turner, and Ashvin Vishwanath for useful comments and acknowledge support from ARO through the OLE program (J.K. and J.E.M), Knut and Alice Wallenberg foundation (J.K.) and WIN (A.E.).

APPENDIX A: THE DIPOLE TERM

The dipolar energy of a magnetized fluid with magnetization $\mathcal{M}(\mathbf{x})$ is

$$\frac{\mu_0}{8\pi} \int d\mathbf{x} d\mathbf{x}' \left[\frac{\mathcal{M} \cdot \mathcal{M}' - 3(\mathcal{M} \cdot \hat{\mathbf{r}})(\mathcal{M}' \cdot \hat{\mathbf{r}})}{r^3} - \frac{8\pi}{3} \mathcal{M}^2 \delta^3(\mathbf{r}) \right],$$

where $\mathbf{r} = \mathbf{x} - \mathbf{x}'$ and $\mathcal{M}' = \mathcal{M}(\mathbf{x}')$. The last term, or “s-wave” part, contributes to the contact interaction c_2 in the BEC Hamiltonian and so should not be treated independently. In this paper we take the first, “d-wave” part to be the full dipolar interaction. This can, in turn, be decomposed into a “Coulomb” part that is positive semidefinite and hence convenient for numerical work that searches for energy minima and a contact part as in Eq. (13).

For both analytical and numerical work we need the dimensionally reduced form of the Coulomb part expressed in a rotating frame. Ignoring the contact term in H_{dip} and performing two partial integrations we find

$$\begin{aligned} E_{dip}^C &= \frac{c_d}{2} \int d^3x d^3x' \frac{\nabla \cdot [n_{3D} \mathbf{M}(\mathbf{x})] \nabla' \cdot [n_{3D} \mathbf{M}(\mathbf{x}')] }{|\mathbf{x} - \mathbf{x}'|} \\ &= \frac{c_d}{2} \int d^2x d^2x' \sigma(x, z) \sigma'(x', z') \int dy dy' \frac{\rho(y) \rho(y')}{|\mathbf{x} - \mathbf{x}'|} \\ &\quad + \frac{c_d}{2} \int d^2x d^2x' n_{2D} M_y(x, z) n_{2D} M_y(x', z') \\ &\quad \times \int dy dy' \frac{[\partial_y \rho(y)] [\partial_{y'} \rho(y')]}{|\mathbf{x} - \mathbf{x}'|} \end{aligned} \quad (\text{A1})$$

where $\sigma(x, z) \equiv \partial_x [n_{2D} M_x(x, z)] + \partial_z [n_{2D} M_z(x, z)]$ is an effective surface-charge density. The density n_{2D} has only a (x, z) dependence for a nonzero trapping potential $U(x, z)$. The integrals over y can be performed explicitly for either Gaussian or boxcar profiles ρ ; we choose the Gaussian form for the purposes of numerics. Then

$$\begin{aligned} \rho(y) \rho(y') &= \frac{2}{\pi \sigma_y^2} e^{-(y_+^2 + y_-^2)/\sigma_y^2}, \\ [\partial_y \rho(y)] [\partial_{y'} \rho(y')] &= \frac{8(y_+^2 - y_-^2)}{\pi \sigma_y^6} e^{-(y_+^2 + y_-^2)/\sigma_y^2}, \end{aligned} \quad (\text{A2})$$

with $y_{\pm} = y \pm y'$. The integrals over y_+ are simple and the integrals over y_- can be put in terms of special functions with help of the identities $\int dx \frac{e^{-x^2}}{\sqrt{c^2 + x^2}} = e^{c^2/2} K_0(\frac{c^2}{2})$ and $\int dx \frac{x^2 e^{-x^2}}{\sqrt{c^2 + x^2}} = \frac{\sqrt{\pi}}{2} U(\frac{1}{2}, 0, c^2)$. Here K_0 is a modified Bessel function and U is a confluent hypergeometric function.

For the numerics, discretize the remaining integrals as follows. Divide the two-dimensional area into rectangular plaquettes and set the density n_{2D} and magnetization \mathbf{M} constant on each plaquette

$$\mathbf{M}(x, z) \rightarrow \mathbf{M} \left[a \left(r + \frac{1}{2} \right), a \left(s + \frac{1}{2} \right) \right], \quad (\text{A3})$$

where a is the lattice constant and r, s are integers. Then do several variable substitutions. Going to variables x_{\pm} and z_{\pm} and scaling the coordinates by a allows us to replace

$$\int d^2x d^2x' \rightarrow \int_{p-1}^{p+1} dx_- \int_{q-1}^{q+1} dz_- (1 - |x_- - p|)(1 - |z_- - q|) \quad (\text{A4})$$

since the integrands depend only on x_- , z_- . Here $p=r'-r$ and $q=s'-s$.

The integrals can then be computed numerically for $0 \leq p, q < \sqrt{N}$. The final step is to time average the fields to take into account the rapid Larmor precession. This effectively means replacing

$$\begin{aligned} \sigma(p, q)\sigma(p', q') &\rightarrow \partial_z[n_{2D}M_z(p, q)]\partial_{z'}[n_{2D}M_z(p', q')] \\ &+ \frac{1}{2}\partial_x[n_{2D}M_x(p, q)]\partial_{x'}[n_{2D}M_x(p', q')] \\ &+ \frac{1}{2}\partial_x[n_{2D}M_y(p, q)]\partial_{x'}[n_{2D}M_y(p', q')] \end{aligned} \quad (\text{A5})$$

and

$$\begin{aligned} M_y(p, q)M_y(p', q') &\rightarrow \frac{1}{2}M_x(p, q)M_x(p', q') \\ &+ \frac{1}{2}M_y(p, q)M_y(p', q') \end{aligned} \quad (\text{A6})$$

in Eq. (A1) since the transverse components rotate into each other but the longitudinal component is unaffected.

APPENDIX B: HELICAL MODULATION

We can obtain a simple estimate of the wavelength of the transverse helical state to leading order in the strength of the dipole coupling by assuming a fully polarized time evolving state $\psi_{\perp}^f(0, k_z z - \gamma B_0 t)$, Eq. (7), with magnetization

$$M_x + iM_y = n_{2D}\rho(y)e^{i(k_z z - \gamma B_0 t)}. \quad (\text{B1})$$

Fourier transforming the kinetic and the dipole energy term, keeping only contributions that scale with the area of the two-dimensional system, the (areal) energy density of this state is

$$\frac{\text{energy}}{\text{area}} = n_{2D} \frac{\hbar^2 k_z^2}{2m} + \frac{c_d n_{2D}^2}{2} \int \frac{dk_y}{2\pi} \frac{4\pi}{k_y^2 + k_z^2} k_y^2 |\tilde{\rho}(k_y)|^2 \quad (\text{B2})$$

plus k_z -independent terms. In the kinetic term, there is a factor of 1/2 because only half the atoms are in the $m_z = \pm 1$ states that carry kinetic energy. In the dipole term, the only extensive contribution to the energy comes from the out-of-plane component M_y , which gives a factor 1/2 there as well. Notice also that the time dependence is gone. With $k_y^2/(k_y^2 + k_z^2) = 1 - k_z^2/(k_y^2 + k_z^2)$, the relevant terms are

$$n_{2D} \frac{\hbar^2 k_z^2}{2m} - \frac{c_d n_{2D}^2}{2} |k_z| \int \frac{du}{2\pi} \frac{4\pi}{1+u^2} |\tilde{\rho}(|k_z|u)|^2 \quad (\text{B3})$$

and to lowest order in k_z we just need $\tilde{\rho}(0) = \int dy \rho(y) = 1$ to arrive at

$$n_{2D} \frac{\hbar^2 k_z^2}{2m} - \frac{c_d}{2} n_{2D}^2 |k_z|, \quad (\text{B4})$$

which takes its minimum at

$$k_z = \pm \frac{\pi n_{2D} c_d}{2 \hbar^2 / 2m}. \quad (\text{B5})$$

APPENDIX C: DIPOLE ENERGY AT UNIFORM MAGNETIZATION

For a uniform condensate with maximal magnetization, aligned parallel to the magnetic field, the only contribution to the dipole energy comes from the edges at $z = \pm L/2$. The second term in Eq. (A1) does not contribute and only the edges of the first

$$\begin{aligned} E_{dip}^C &= \frac{c_d n_{2D}^2}{2} \int_{-W/2}^{W/2} dx dx' \int_{-\infty}^{\infty} dy dy' \rho(y) \rho(y') \\ &\times 2 \left[\frac{1}{\sqrt{x_-^2 + y_-^2}} - \frac{1}{\sqrt{x_-^2 + y_-^2 + L^2}} \right]. \end{aligned} \quad (\text{C1})$$

In the limit $L \gg W \gg T$, the leading contribution to the energy comes solely from the first term, which describes the self-energy of two quasi-one-dimensional lines of charge. Indeed, it becomes just

$$E_{dip}^C = 2c_d n_{2D}^2 \int dx_- (W - x_-)/x_- = 2c_d n_{2D}^2 W \ln W/T + O(W) \quad (\text{C2})$$

asymptotically, where the lower cutoff T has been chosen for convenience.

The energy for the uniform out-of-plane configuration is

$$E_{dip}^C = \frac{c_d}{2} n_{2D}^2 \int d^3x d^3x' \frac{[\partial_y \rho(y)][\partial_{y'} \rho(y')]}{|\mathbf{x} - \mathbf{x}'|}. \quad (\text{C3})$$

Since there will be a term extensive in the planar size, it is simplest to ignore the effects of boundaries and work with a surface energy density

$$\begin{aligned} \eta &= \frac{c_d}{2} n_{2D}^2 2\pi \int dy dy' \int_0^R dr \frac{r[\partial_y \rho(y)][\partial_{y'} \rho(y')]}{\sqrt{r^2 + y_-^2}} \\ &= 2\pi c_d n_{2D}^2 \int dy dy' \rho(y) \rho(y') \delta(y - y') + O(1/R) \\ &= 2\pi c_d n_{2D}^2 \frac{1}{T} \end{aligned} \quad (\text{C4})$$

after integrating over the radial coordinate r followed by partial integration in y and y' .

- ¹L. Sadler, J. Higbie, S. R. Leslie, M. Vengalattore, and D. M. Stamper-Kurn, *Nature (London)* **443**, 312 (2006).
- ²M. Vengalattore, S. R. Leslie, J. Guzman, and D. M. Stamper-Kurn, *Phys. Rev. Lett.* **100**, 170403 (2008).
- ³M. Vengalattore, J. Guzman, S. Leslie, F. Serwane, and D. M. Stamper-Kurn, arXiv:0901.3800 (unpublished).
- ⁴E. Kim and M. H. V. Chan, *Nature (London)* **427**, 225 (2004).
- ⁵C. W. Cherng and E. Demler, *Phys. Rev. Lett.* **103**, 185301 (2009).
- ⁶A. Lamacraft, *Phys. Rev. A* **77**, 063622 (2008).
- ⁷J. D. Sau, S. R. Leslie, D. M. Stamper-Kurn, and M. L. Cohen, *Phys. Rev. A* **80**, 023622 (2009).
- ⁸T.-L. Ho, *Phys. Rev. Lett.* **81**, 742 (1998).
- ⁹T. Ohmi and K. Machida, *J. Phys. Soc. Jpn.* **67**, 1822 (1998).
- ¹⁰S. Mukerjee, C. Xu, and J. E. Moore, *Phys. Rev. B* **76**, 104519 (2007).
- ¹¹D. Podolsky, S. Chandrasekharan, and A. Vishwanath, arXiv:0707.0695 (unpublished).
- ¹²E. G. M. van Kempen, S. J. J. M. F. Kokkelmans, D. J. Heinzen, and B. J. Verhaar, *Phys. Rev. Lett.* **88**, 093201 (2002).
- ¹³Discussion with D. M. Stamper-Kurns experimental group at Berkeley.
- ¹⁴A. Griesmaier, J. Werner, S. Hensler, J. Stuhler, and T. Pfau, *Phys. Rev. Lett.* **94**, 160401 (2005).
- ¹⁵S. Mukerjee, C. Xu, and J. E. Moore, *Phys. Rev. Lett.* **97**, 120406 (2006).
- ¹⁶F. Zhou, *Phys. Rev. Lett.* **87**, 080401 (2001).
- ¹⁷C. Kittel, *Phys. Rev.* **70**, 965 (1946).
- ¹⁸N. Metropolis, A. W. Rosenbluth, M. N. Rosenbluth, A. H. Teller, and E. Teller, *J. Chem. Phys.* **21**, 1087 (1953).
- ¹⁹C. Trefzger, C. Menotti, and M. Lewenstein, *Phys. Rev. A* **78**, 043604 (2008).
- ²⁰J. Zhang and T.-L. Ho, arXiv:0908.1593 (unpublished).
- ²¹Y. Kawaguchi, H. Saito, K. Kudo, and M. Ueda, arXiv:0909.0565 (unpublished).